Regularization Designs for Uniform Spatial Resolution and Noise Properties in Statistical Image Reconstruction for 3D X-ray CT: Supplementary Material

Jang Hwan Cho, *Student Member, IEEE,* and Jeffrey A. Fessler, *Fellow, IEEE*

This material extends the regularization designs investigated in [1], and presents the simulation and clinical experiments that supports the results in [1] or were excluded in [1] due to their repetitive nature.

Numberings for figures, tables, and equations are continuous from [1], and reference to bibiography is within this material.

I. Images for the pre-tuned spatial strength

In this section, we compare the pre-tuned spatial strengths introduced in [1], for the clinical data.

Fig. 9 shows the pre-tuned spatial strength $\{\kappa_j\}$ of A-REG, defined as (6), at xy, xz, and yz planes through the image center. The image shows the entire trans-axial field-of-view (FOV), which is 70 cm. Notice that a cylindrical mask was used.

Fig. 10 compares the pre-tuned spatial strengths for A-REG, R-REG, and N-REG at both a center slice and an end slice. The pre-tuned spatial strengths contain object information and is smooth. We can verify that the approximation $\kappa_j \approx \kappa_l$ for l within the neighborhood of j is reasonable. Since the measurements are obtained from the short-scan protocol, end slices suffer from insufficient sampling at certain locations. The regularization strengths at such locations become overly smoothed and lose object information reflecting their sampling conditions.

Fig. 12 compares x profiles through the center of the pre-tuned spatial strengths for A-REG, R-REG, and N-REG. We can see that R-REG assigns smaller regularization strength to undersampled region compared to A-REG. N-REG has smaller dynamic range for the regularization strength compared to others due to the square root (51).

The approximation in (39) was evaluated empirically in Fig. 11 and Fig. 13. We can observe that the approximation holds reasonably well. Notice that ripple-like structures in Fig. 11 (a) are disappeared in Fig. 11 (b) .

The approximation in (37) was also evaluated empirically in Fig. 14. We compared (36) and (38) by calculating the ratio

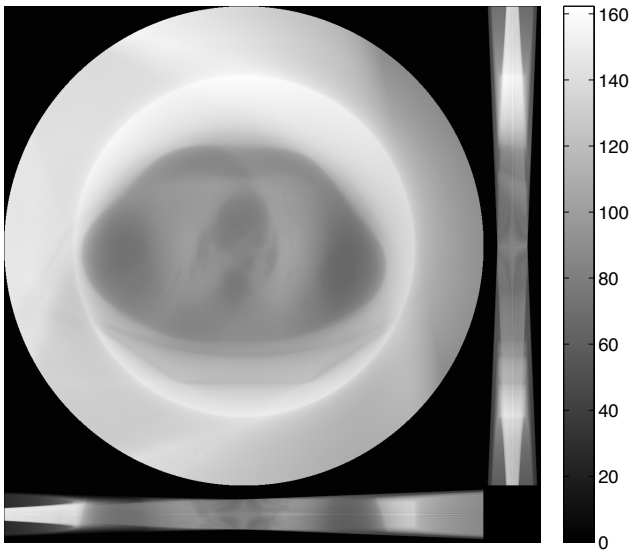

Fig. 9. Middle 3 planes of the pre-tuned spatial strength (6) (xy, xz, and yz planes through the image center).

in (36),

$$\text{ratio} = \frac{\sqrt{\Re_+(\langle R_\omega F\left(\boldsymbol{G}'\boldsymbol{G}\boldsymbol{\delta}_{\text{ref}}\right), R_\omega F\left(\boldsymbol{G}'\boldsymbol{G}\boldsymbol{\delta}_j\right)\rangle)}}{\|R_\omega F\left(\boldsymbol{G}'\boldsymbol{G}\boldsymbol{\delta}_{\text{ref}}\right)\|}. \quad (55)$$

We simulated a 64-slice CT scanner, which has 40 mm detector coverage. To simplify the experiment, we down sampled the system by a factor of 4 from a conventional setup, and only presented the ratio (55) along the positive x axis at $y = 0(mm)$ and $z = 1.25$, 11.25, and 21.25 (mm). Notice that the slice at $z = 21.25$ (mm) is slightly outside the detector coverage. The approximation holds well near center slices, but becomes less accurate for slices away from the center. The result suggests that the approximation (37) is somewhat inaccurate for voxels away from the reference point, and the hypothetical geometry $\boldsymbol{G}$ need to be designed more sophisticatedly. However, if we calculate the ratio (55) using the system matrix $\boldsymbol{A}$ (by simply replacing $\boldsymbol{G}$ with $\boldsymbol{A}$), we can observe that the hypothetical geometry $\boldsymbol{G}$ gives more "shift-invariant" $\boldsymbol{G}'\boldsymbol{G}$ as intended (see Fig. 14) .

II. Selection of the hypothetical geometry

In [1], new regularizers for uniform resolution or noise were derived using a hypothetical geometry $\boldsymbol{G}$, which was assumed

This work was supported in part by GE Healthcare and CPU donation from Intel Corporation.

Jang Hwan Cho and Jeffrey A. Fessler are with the Department of Electrical Engineering and Computer Science, University of Michigan, Ann Arbor, MI 48105 USA (e-mail: janghcho@umich.edu, fessler@umich.edu).

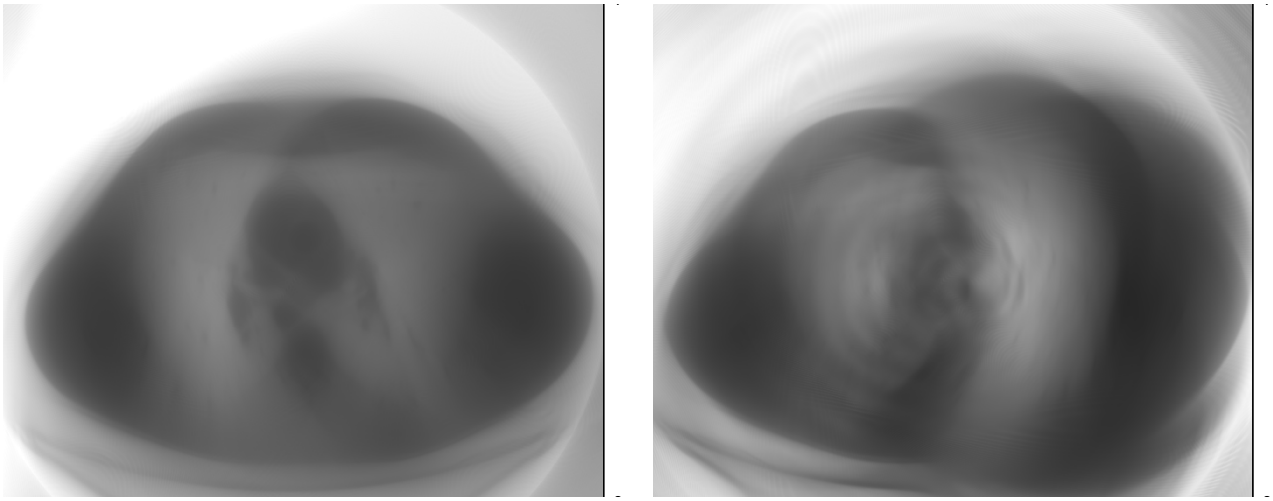

(a) A-REG (6)

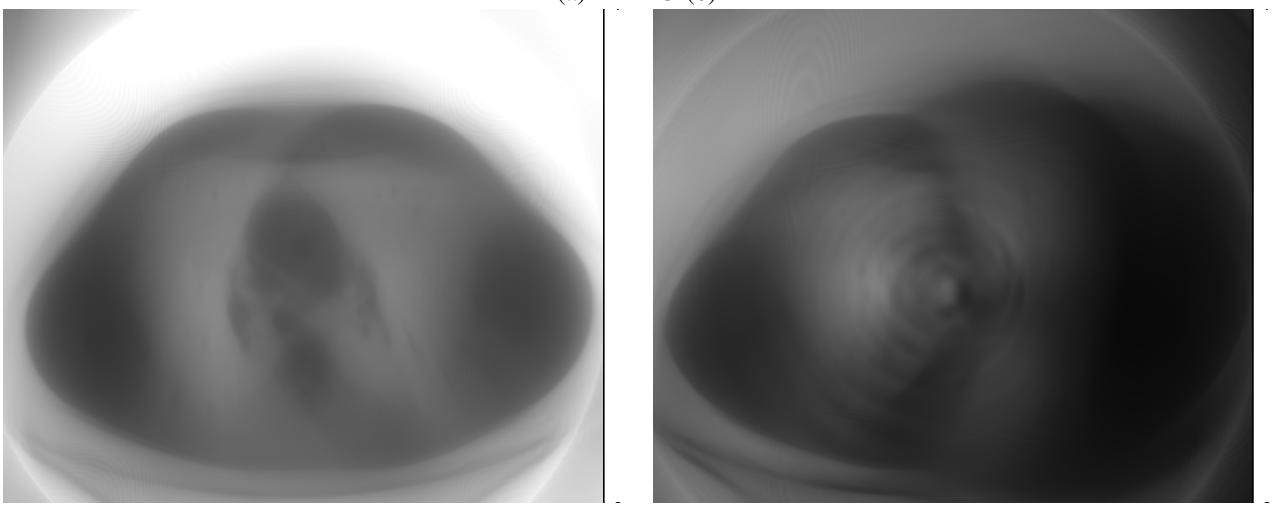

(b) R-REG (38)

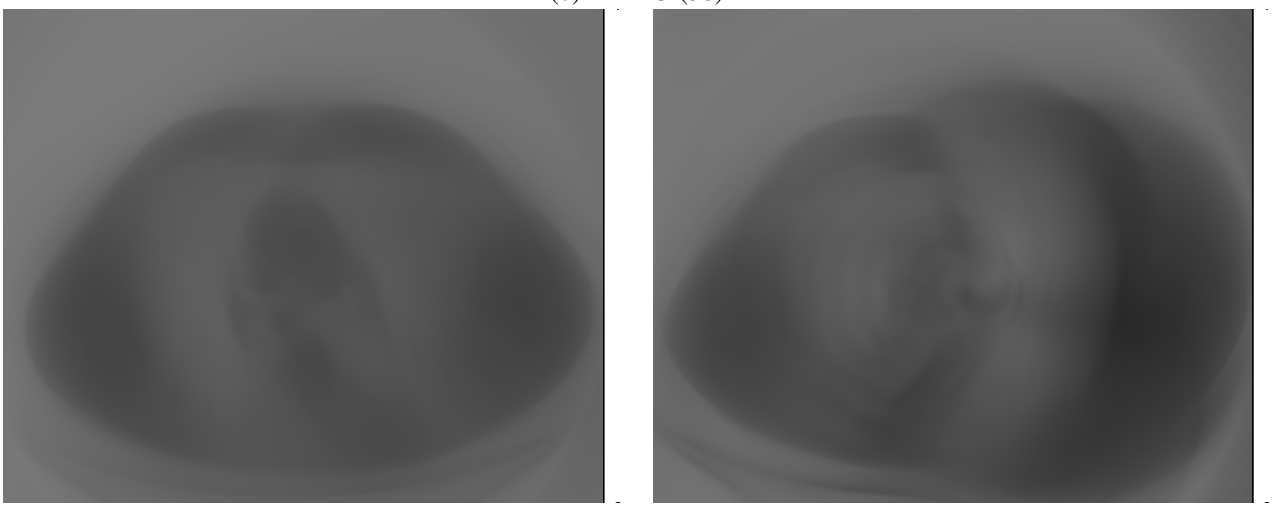

(c) N-REG (51)

Fig. 10. Comparison of the pre-tuned spatial strengths for A-REG, R-REG, and N-REG at a center slice (left column) and an end slice (right column). Display range is [0 250].

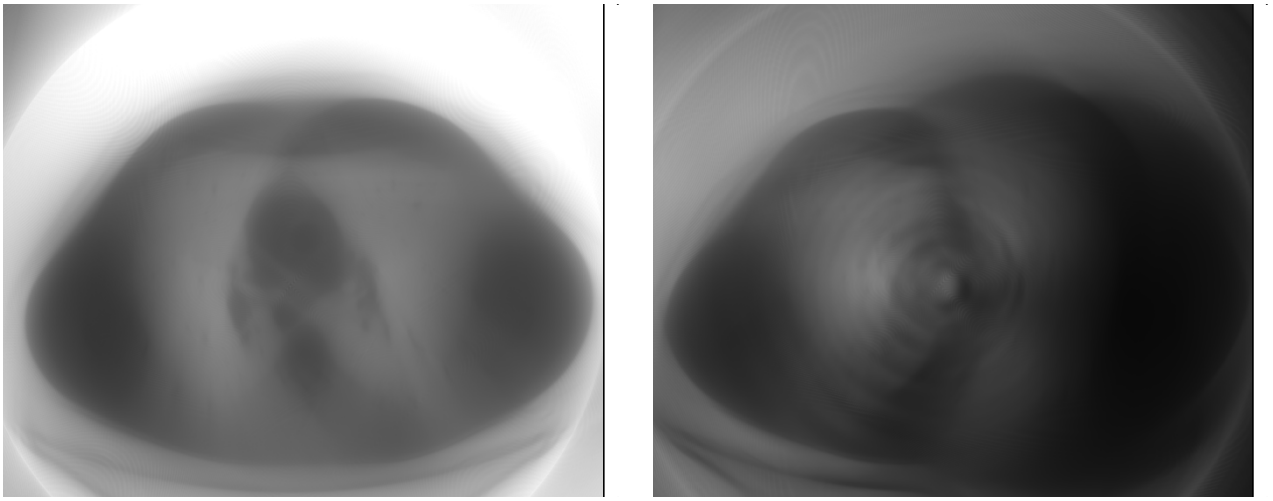

(a) R-REG (38)

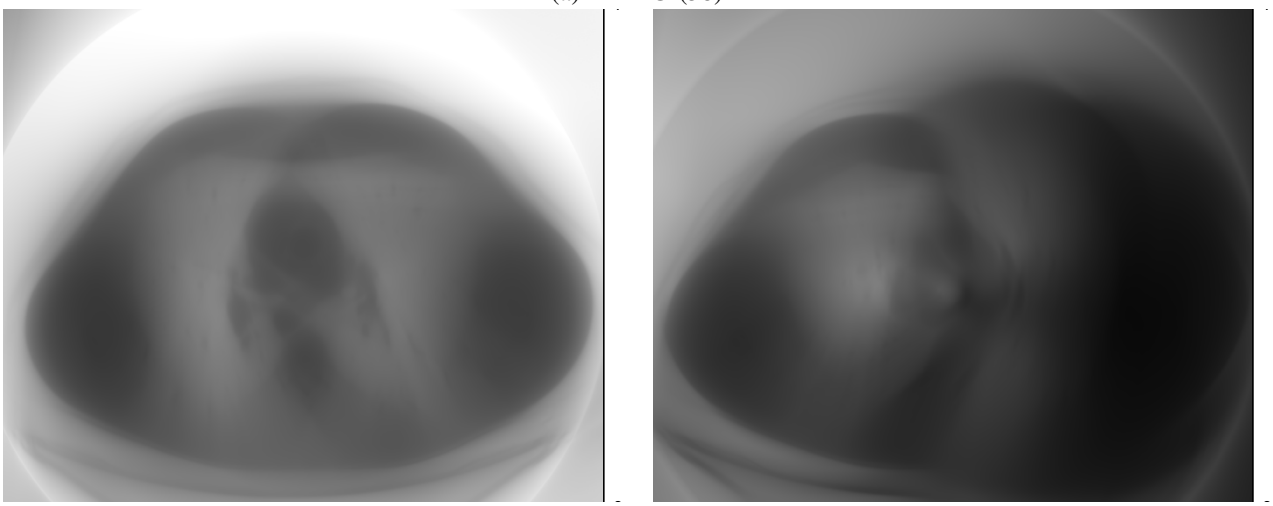

(b) Approximated R-REG (39)

Fig. 11. Comparison of the pre-tuned spatial strengths for R-REG and its approximation given in (38) at a center slice (left column) and an end slice (right column). Display range is [0 250].

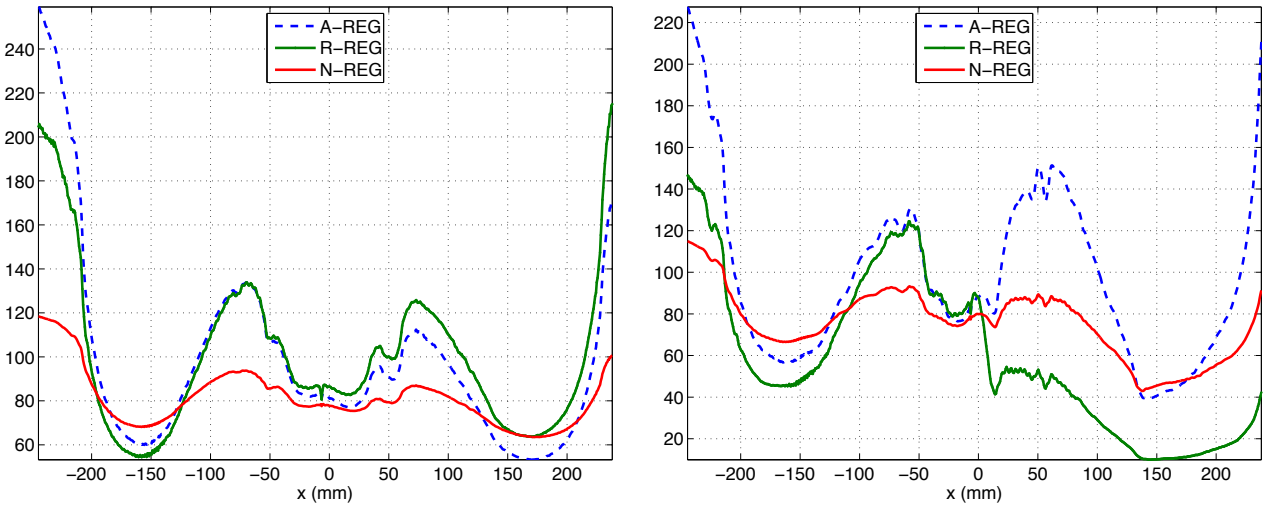

Fig. 12. Comparison of x profiles through the center of the pre-tuned spatial strengths for A-REG, R-REG, and N-REG. From center slice (left) and end slice (right).

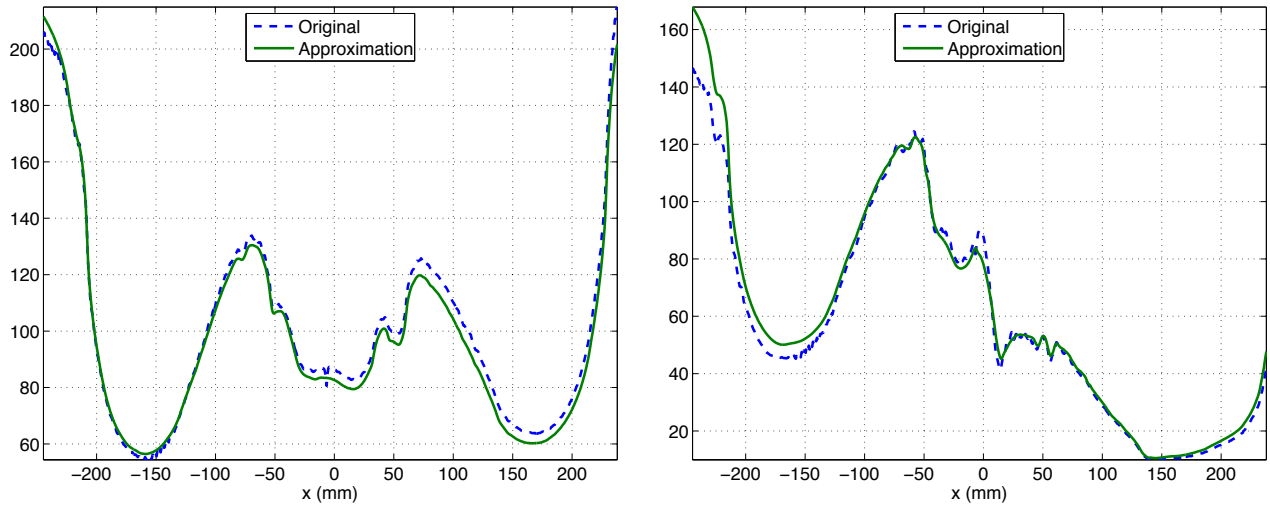

Fig. 13. Comparison of x profiles through the center of the pre-tuned spatial strength (38) and its approximation (39). From center slice (left) and end slice (right).

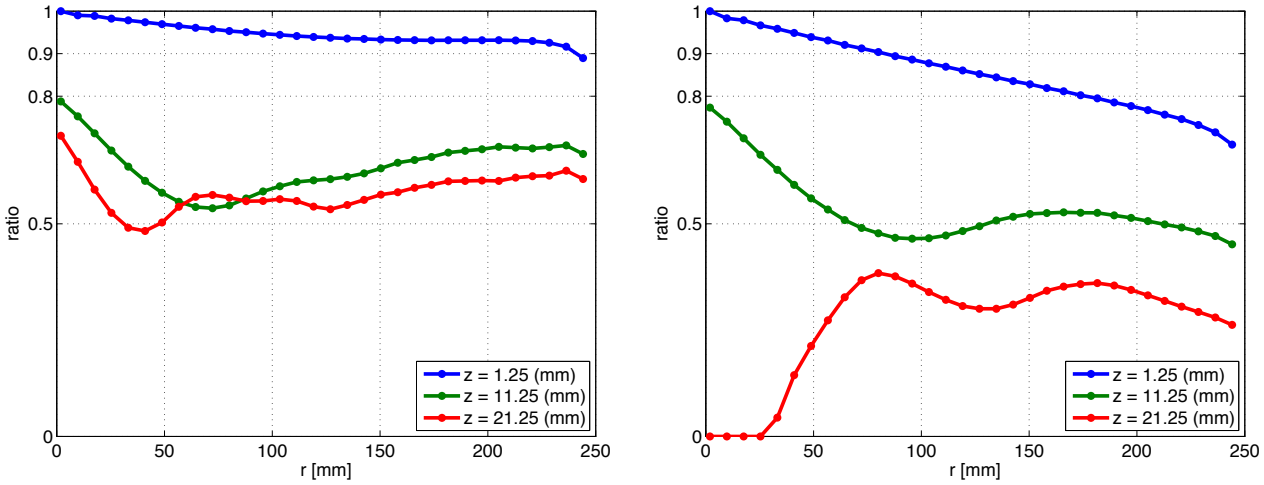

Fig. 14. Plot of (55) along the positive x axis at $y = 0$ (mm) and $z = 1.25, 11.25, 21.25$ (mm), with the hypothetical geometry $\boldsymbol{G}$ used in [1] (left) and with the system matrix $\boldsymbol{A}$ replacing $\boldsymbol{G}$ in (55) (right).

to be an ideal and fully sampled geometry. In practice, the choice of $\boldsymbol{G}$ affects how closely the regularizer can achieve the uniformity of resolution or noise. For the experiments in [1], $\boldsymbol{G}$ was chosen to be a hypothetical cone-beam CT geometry with large enough number of detector rows and 360° orbit, and both the ray dependent factor c_i and the voxel dependent factor s_j were assumed to be 1 for every location. Because of the cone-angle, such hypothetical geometry $\boldsymbol{G}$ does not provide perfectly shift-invariant $\boldsymbol{G}'\boldsymbol{G}$, even though it is "more shift-invariant" compared to $\boldsymbol{A}'\boldsymbol{A}$. This geometry with extended views and rows was one of the most intuitive choices for $\boldsymbol{G}$, and now we investigate an alternate decomposition in this supplement.

We let the hypothetical geometry described above as $\boldsymbol{A}_{\text{ext}} = \{\hat{a}_{ij}\}$, then it can be further factorized as follows

$$\hat{a}_{ij} = g_{ij}\hat{s}_j, \tag{56}$$

so that we obtain

$$g_{ij} = \frac{\hat{a}_{ij}}{\hat{s}_j}, \tag{57}$$

where $\hat{s}_j$ is a voxel-dependent factor that provides another choice for $\boldsymbol{G} = \{g_{ij}\}$. Intuitively, we want to design $\{\hat{s}_j\}$ such that $\boldsymbol{G}'\boldsymbol{G}$ has constant diagonal elements. Defining

$$\hat{s}_j = \sqrt{\sum_{i=1}^{N_{\text{g}}} \hat{a}_{ij}^2} \tag{58}$$

yields $[\boldsymbol{G}'\boldsymbol{G}]_{jj} = 1, \ \forall j$. Using above designs, we obtain the following matrix representation for the system matrix $\boldsymbol{A}$

$$\boldsymbol{A} = \boldsymbol{P}\boldsymbol{G}\boldsymbol{D}[\hat{s}_j], \tag{59}$$

where $\boldsymbol{P}$ is defined in [1], and c_i was assumed to be 1 for every detector element. The Fisher information matrix can be approximated as (20) with the following new expressions for

TABLE IV
ACRONYM SUFFIXES FOR REGULARIZERS

Suffix	Description
-1	regularizers designed by selecting the hypothetical geometry with extended views and rows as $\boldsymbol{G}$ and $s_j = 1, \forall j$
-2	regularizers designed by using the system matrix factorization in (59)

(22) and (23):

$$\eta_j = \sqrt{\frac{\sum_{i=1}^{n_\mathrm{d}} g_{ij}^2 w_i}{\sum_{i=1}^{N_\mathrm{g}} g_{ij}^2}} = \sqrt{\sum_{i=1}^{n_\mathrm{d}} g_{ij}^2 w_i}, \tag{60}$$

$$\lambda_j = s_j \eta_j = \sqrt{\sum_{i=1}^{n_\mathrm{d}} \hat{a}_{ij}^2 w_i} = \sqrt{\sum_{i=1}^{n_\mathrm{d}} a_{ij}^2 w_i}. \tag{61}$$

Notice that (61) no longer depends on the hypothetical geometry $\boldsymbol{G}$ explicitly and requires less computation compared to both the original certainty (6) and the modified pre-tuned spatial strength (23).

New approximation (59) for the Fisher information matrix leads to different regularizers from those we used for the experiments in [1] (see Table I and Table IV for acronyms). The main purpose of this supplementary material is to compare these regularizers obtained from different system matrix factorization. Since the derivation for both proposed regularizers in [1] is general, new regularizers are readily obtained from (36) and (49).

A. Regularizer for uniform spatial resolution

New regularizer for uniform spatial resolution is obtained by substituting $\boldsymbol{G}$ from (59) and (61) into (36). Using the shift-invariant approximation (37), the new regularizer for spatial resolution uniformity (hereafter R-REG-2) can be written as (5) with

$$\hat{\kappa}_j = \sqrt{\sum_{i=1}^{n_\mathrm{d}} a_{ij}^2 w_i}. \tag{62}$$

For practical implementation as described in [1], we approximate (62) as follows

$$\hat{\kappa}_j \approx \gamma \sqrt{\sum_{i=1}^{n_\mathrm{d}} a_{ij} w_i}, \tag{63}$$

where the approximation requires a proper scaling factor γ. The approximation scaling factor γ can be obtained manually or by matching both sides of (62) at a reference point, *i.e.*,

$$\gamma = \sqrt{\left[\sum_{i=1}^{n_\mathrm{d}} a_{ij}^2 w_i\right]_{j=j_\mathrm{ref}} \Big/ \left[\sum_{i=1}^{n_\mathrm{d}} a_{ij} w_i\right]_{j=j_\mathrm{ref}}}, \tag{64}$$

where j_ref indicates the lexicographical index of the reference location.

The new regularizer R-REG-2 (62) does not have a normalization or a denominator, which also leads to decreased regularization strength for under-sampled region compared to the original certainty (6). Both designs (38) and (62) are expected to have similar effects to the reconstructed image, but possibly with different amount.

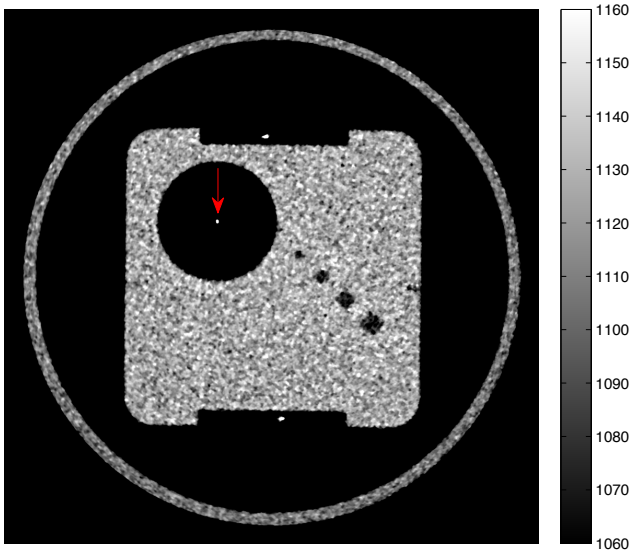

Fig. 15. The GEPP phantom used for quantitative comparison of regularizers. Red arrow indicate tungsten wire used for spatial resolution comparison.

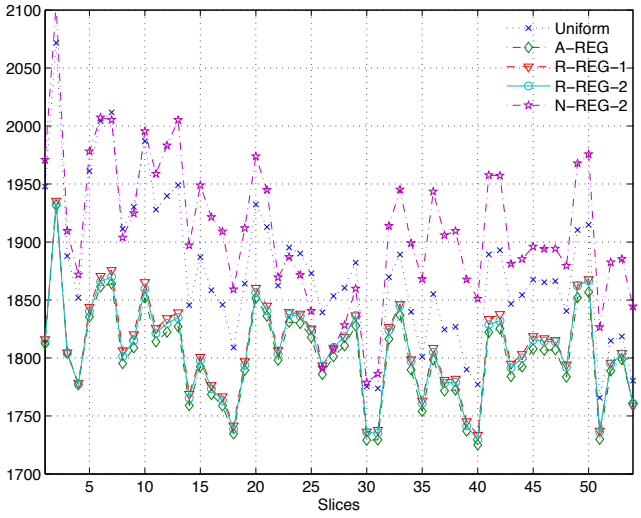

Fig. 16. Comparison of the peak value of the tungsten wire in GEPP for the following regularizers: Uniform, A-REG, R-REG-1, R-REG-2, and N-REG-2.

B. Regularizer for uniform noise property

Substituting (59) into (17) leads to the following new expressions for (41) and (42)

$$\bar{\lambda}_j \triangleq \sqrt{\sum_{i=1}^{n_\mathrm{d}} a_{ij}^2 \hat{w}_i v_i}, \quad \bar{\Lambda} \triangleq \boldsymbol{D}[\bar{\lambda}_j], \tag{65}$$

$$\hat{\lambda}_j \triangleq \sqrt{\sum_{i=1}^{n_\mathrm{d}} a_{ij}^2 \hat{w}_i v_i^2}, \quad \hat{\Lambda} \triangleq \boldsymbol{D}[\hat{\lambda}_j]. \tag{66}$$

Substituting $\boldsymbol{G}$ from (59), (65) and (66) into (51) yields a new regularizer for noise uniformity (hereafter N-REG-2).

TABLE V
AVERAGE CRC MISMATCH (52) FOR SELECTED 6 LOCATIONS ACROSS SLICES AND WITHIN EACH SLICE, RESPECTIVELY (UNITS: %). SEE FIG. 1 IN [1] FOR THE INDEX OF IMPULSE LOCATIONS.

	Locations						Averages			
	1	2	3	4	5	6	Overall	Center Slice	1st slice of ROI	Outside ROI
A-REG (Fig. 24)	32.6	45.3	24.8	47.2	31.9	25.0	34.5	(a) 12.3	(b) 33.7	(c) 46.8
R-REG-1 (Fig. 3)	7.5	14.9	3.9	20.0	5.9	7.2	9.9	(d) 8.7	(e) 11.6	(f) 7.4
R-REG-2 (Fig. 24)	11.0	18.7	3.9	23.3	9.7	9.4	12.7	(d) 12.1	(e) 14.4	(f) 10.4
A-REG (Fig. 26)	31.3	44.1	21.9	47.9	33.4	20.6	33.2	(a) 11.9	(b) 34.5	(c) 44.9
R-REG-1 (Fig. 22)	9.5	14.3	2.9	21.5	9.8	7.1	10.9	(d) 10.5	(e) 14.6	(f) 9.1
R-REG-2 (Fig. 26)	11.5	18.1	2.5	24.8	11.9	7.4	12.7	(d) 12.9	(e) 17.0	(f) 9.2

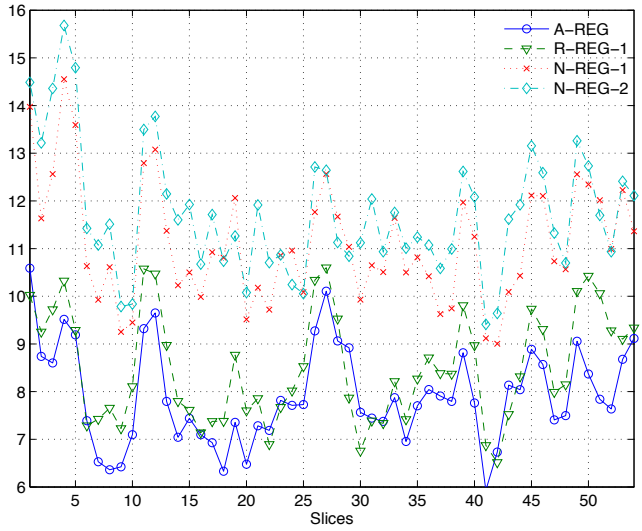

Fig. 17. Comparison of the noise standard deviation in a homogeneous region of the GEPP, which corresponds to the left phantom wall in Table. III, for the following regularizers: A-REG, R-REG-1, N-REG-1, and N-REG-2.

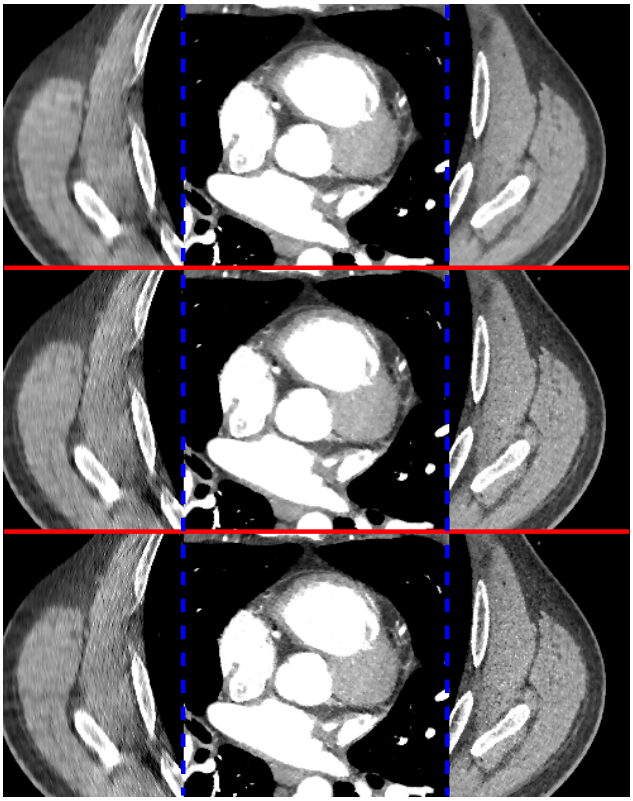

Fig. 18. Comparison of reconstructed images obtained from A-REG (top), R-REG-1 (middle) and R-REG-2 (bottom) at 3 selected locations (separated by blue dash lines) on the last slice of ROI. Display window is [800 1200] (HU).

III. COMPARISON BETWEEN REGULARIZERS FROM DIFFERENT SYSTEM MATRIX FACTORIZATIONS

A. Physical Phantom Experiment

We used the GE performance phantom (GEPP) to compare the resolution properties of the reconstructed image from different regularizations. The phantom was scanned and reconstructed as described in [1]. The GEPP has a tungsten wire in water as indicated in Fig. 15, and its peak values in each slice of the reconstructed image will be used to assess resolution uniformity.

In Fig. 16, we compare the peak value of the tungsten wire profile at every ROI slice for the following regularizers: Uniform, A-REG, R-REG-1,R-REG-2, and N-REG-2. Notice that on center slices all the regularizers generate similar peak values for the tungsten wire due to matched regularization strength at the isocenter. Uniform regularizer and proposed regularizer N-REG-2 for noise uniformity induce non-uniform spatial resolution characteristics to the reconstructed image, which result in widely varying peak values of the tungsten wire. The standard deviation in the peak value is approximately 64 HU for these regularizations. On the other hand, the other 3 regularizers aimed for spatial resolution uniformity show much better performances as shown in Fig. 16, and have approximately 40 HU standard deviation in the peak value. Due to small FOV (23 cm) and its location, the sampling condition of the tungsten wire is approximately the same for every slices, thus both proposed regularizers R-REG-1 and R-REG-2 perform almost the same as A-REG.

Fig. 17 compares the noise standard deviation in a homogeneous region of the GEPP, which corresponds to the left phantom wall in Table. III, for the following regulairzers: A-REG, R-REG-1, N-REG-1 and N-REG-2. A-REG and R-REG-1 show over-regularizing behavior for given location. On the other hand, both proposed regularizers for uniform noise, N-REG-1 and N-REG-2, show improved noise uniformity. Overall performances of N-REG-1 and N-REG-2 are very similar, but show differences for some slices.

B. XCAT Phantom Simulation

We used the XCAT phantom to illustrate the performance of the proposed regularizer R-REG-2 (62). The same simulation

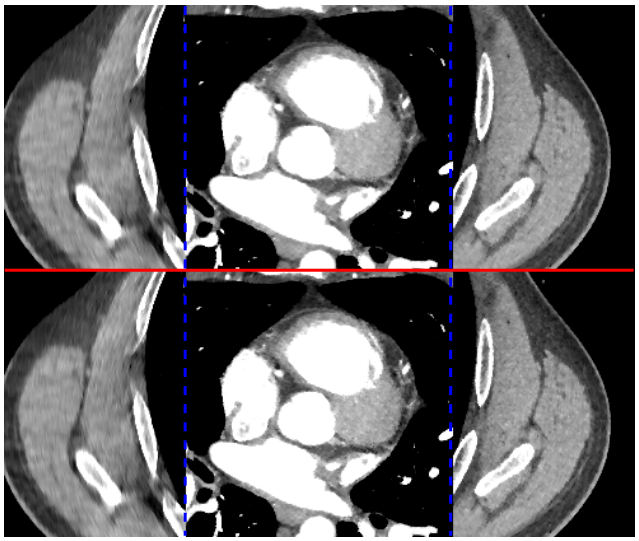

Fig. 19. Comparison of reconstructed images obtained from both uniform noise regularizers, N-REG-1 (top) and N-REG-2 (bottom), at 3 selected locations (separated by blue dash lines) on the 1st slice of ROI. Display window is [800 1200] (HU).

settings as in [1] have been used. The improvements in the spatial resolution uniformity were demonstrated by comparing the impulse responses at different voxel locations obtained by using A-REG (6) to that of the proposed regularizer R-REG-2.

Results for both quadratic and edge-preserving regularizations are presented from Fig. 23 to Fig. 26. We also present the result for R-REG-1 with edge-preserving regularization in Fig. 21 and Fig. 22. Similar to the results with R-REG-1 (38), the proposed regularizer R-REG-2 (62) effectively generate spatially uniform resolution in terms of the constant recovery constant (CRC). Table V compares CRC mismatch (52) of A-REG, R-REG-1, and R-REG-2. R-REG-2 improves the average CRC mismatch by approximately 20% throughout the image volume. Both R-REG-1 and R-REG-2 show comparable performances of improving the resolution uniformity, but R-REG-1 is slightly better.

C. Real Clinical Data

Same clinical cardiac CT scan used in [1] was reconstructed with various regularizers. Fig. 18 compares reconstructed images obtained from both proposed regularizers for resolution uniformity, R-REG-1 and R-REG-2. The reconstructed image using A-REG was presented as a reference. Reconstructed image from R-REG-2 is slightly more shaper and noisier compared to that of R-REG-1 on end slices, but they show very similar image characteristics overall. Fig. 19 compares reconstructed images from proposed uniform noise regularizers, N-REG-1 and N-REG-2, and they have very comparable visual image quality.

IV. Compromise Regularizer

As illustrated on previous sections, each proposed regularizer, either aiming for uniform resolution or noise characteristics, reasonably achieves its goal. However, due to the trade-off between these image quality properties, using one of these regularizations may not provide the "most desirable image", especially near the end slices with sampling issues. Since the readability of the reconstructed image depend on many factors, including both spatial resolution and noise, it is hard to design the optimal regularizer using one criterion. Furthermore, clinicians may have different preferences for the appearance of the reconstructed image, complicating the regularization design process.

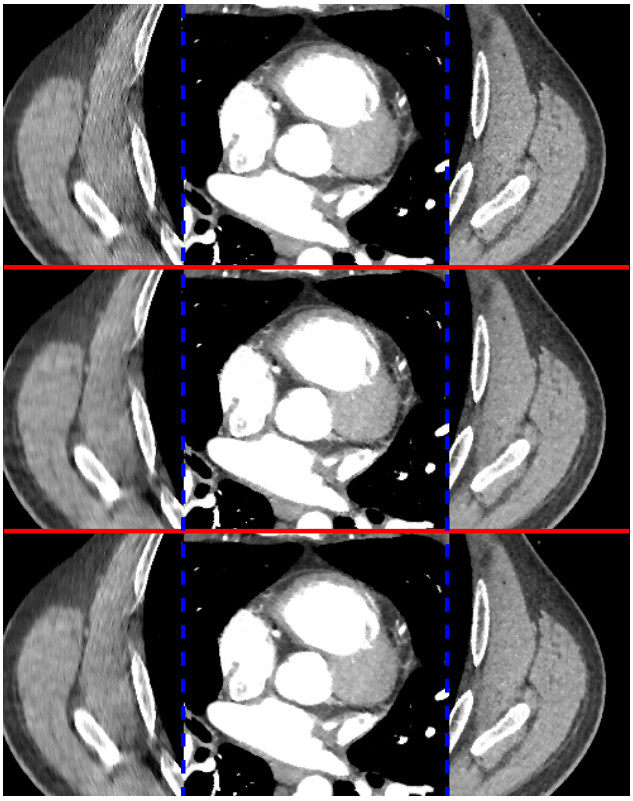

Fig. 20. Comparison of reconstructed images obtained using R-REG-1 (top), N-REG-1 (middle) and compromise regularizer (bottom) at 3 selected locations (separated by blue dash lines) on the last slice of ROI. Display window is [800 1200] (HU).

We investigated a "compromise" regularizer whose pre-tuned spatial strength function κ_j is the arithmetic average of (38) and (51). This simple extension of proposed methods gives a sub-optimal solution for the trade-off between spatial resolution and noise property.

Table VI shows that the compromise regularizer provides the noise uniformity in between those of R-REG-1 and N-REG-1, as expected. Fig. 20 compares the reconstructed images from following regularizers: R-REG-1, N-REG-1, and compromise regularizer. When undersampled region (left column in Fig. 20) is compared, the reconstructed image from compromise reconstruction shows somewhat balanced image quality in spatial resolution and noise properties. However, such improvements are rather subtle.

V. Summary

We presented and compared images of the pre-tuned spatial strengths introduced in [1]. The effect of using the hypothetical geometry and the difference between the proposed designs

TABLE VI
COMPARISON OF THE NOISE STANDARD DEVIATION FOR DIFFERENT REGULARIZERS METHOD. ALL VALUES ARE IN HOUNSFIELD UNITS (HU).

	Uniform	A-REG	R-REG-1	R-REG-2	N-REG-1	N-REG-2	Compromise
Plexiglas^{TM} Insert (center)	14.0	13.7	13.7	13.7	13.6	13.3	13.2
Plexiglas^{TM} Insert (right)	18.8	16.0	16.2	15.8	16.4	16.4	15.8
Plexiglas^{TM} Insert (left)	15.1	14.4	14.5	14.7	14.9	14.7	14.2
Phantom Wall (left)	15.4	9.3	9.5	10.0	11.8	12.7	9.2
Phantom Wall (right)	16.9	8.8	6.8	7.4	10.1	10.1	8.3
Phantom Wall (top)	17.4	8.7	8.8	7.6	10.7	10.6	8.6
Phantom Wall (bottom)	16.1	7.7	8.8	9.0	10.9	10.9	9.6
Average	16.2 $\pm$ 1.6	11.2 $\pm$ 3.4	11.2 $\pm$ 3.6	11.2 $\pm$ 3.5	12.6 $\pm$ 2.4	12.7 $\pm$ 2.3	11.3 $\pm$ 3.1

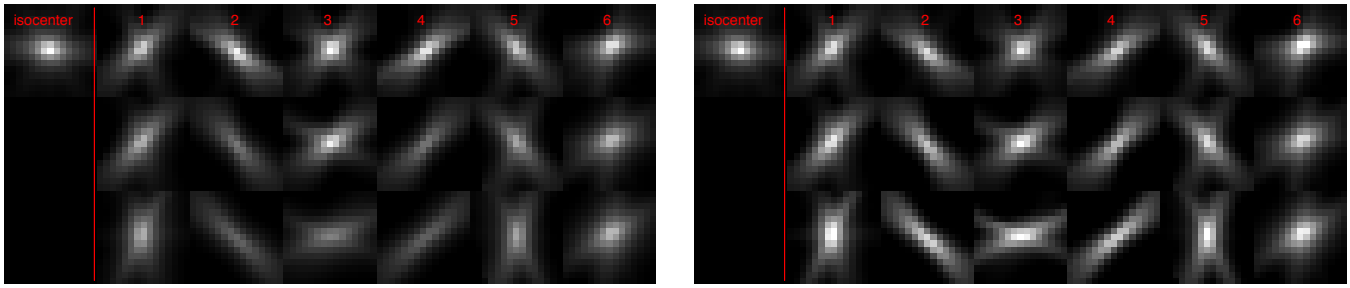

(a) A-REG (b) R-REG

Fig. 21. Comparison of xy plane through the center of each local impulse response at selected location (see Fig.1 for the index of locations). Edge-preserving potential function was used. Top row is from a center slice, middle row is from 1st slice of ROI, and bottom row is from outside ROI. (a) Regularization with original aggregated certainty (6) (A-REG) (b) Regularization with proposed pre-tuned spatial strength (38) (R-REG-1).

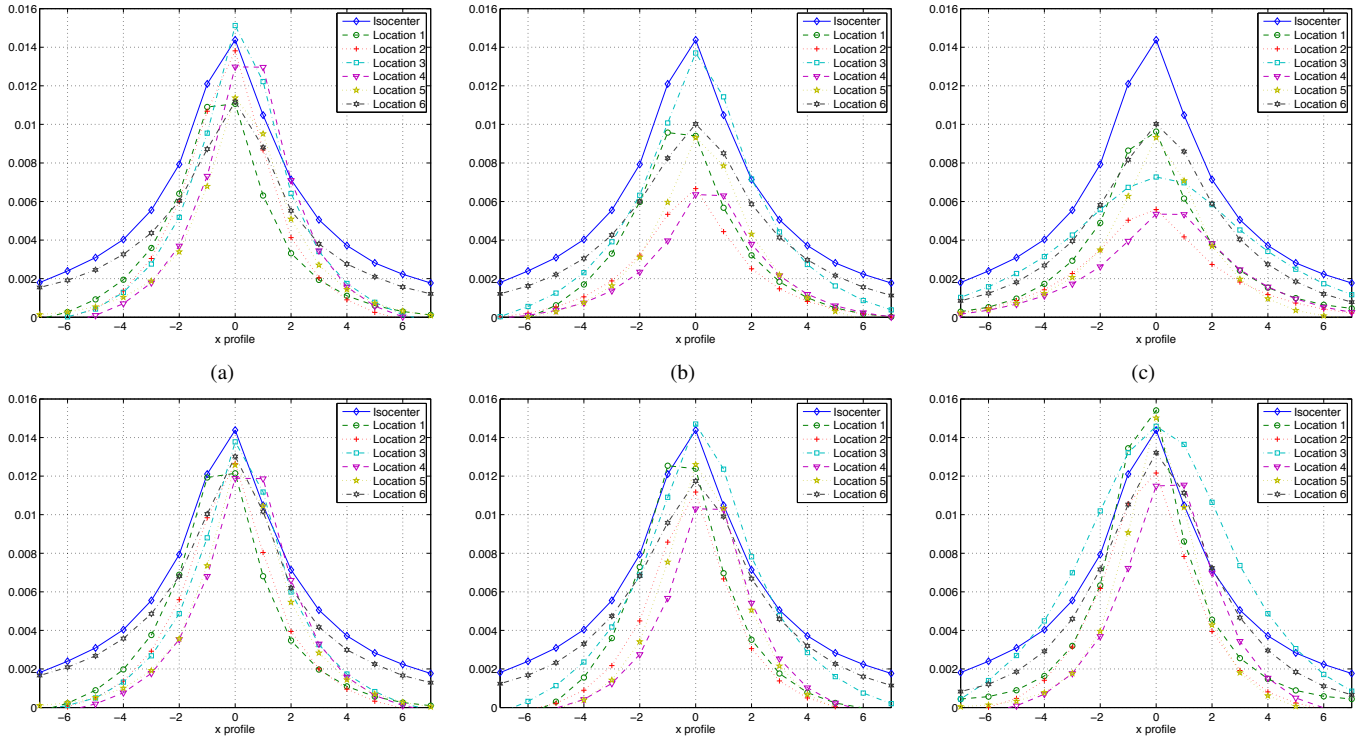

(a) (b) (c)

(d) (e) (f)

Fig. 22. Comparison of x profiles through the center of each impulse response in Fig. 21. Left column is from a center slice, middle column is from 1st slice of ROI, and right column is from outside of ROI. Top and bottom rows represent the regularizers A-REG (6) and the proposed R-REG-1 (38), respectively. (a) A-REG, center slice (b) A-REG, 1st slice of ROI (c) A-REG, outside ROI (d) R-REG-1, center slice (e) R-REG-1, 1st slice of ROI (f) R-REG-1, outside ROI.

were visualized. Presented images also empirically verified approximations (39) in [1].

The choice of the hypothetical geometry $\boldsymbol{G}$ affects the performance of the regularizers that we proposed in [1]. In addition to an intuitive selection we made in [1], we presented another factorization for the system model in this

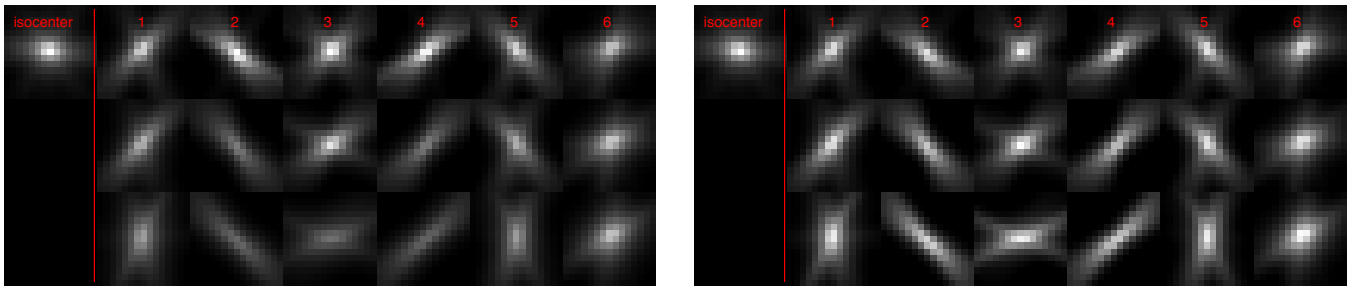

(a) A-REG (b) R-REG-2

Fig. 23. Comparison of xy plane through the center of each local impulses responses at selected location (see Fig. 1 in [1] for the index of locations). Quadratic penalty function was used. Top row is from a center slice (blue line in Fig. 1 in [1]), middle row is from 1st slice of ROI (red line), and bottom row is from outside ROI (green line). (a) Regularization with original aggregated certainty (6) (A-REG) (b) Regularization with proposed pre-tuned spatial strength (62) (R-REG-2).

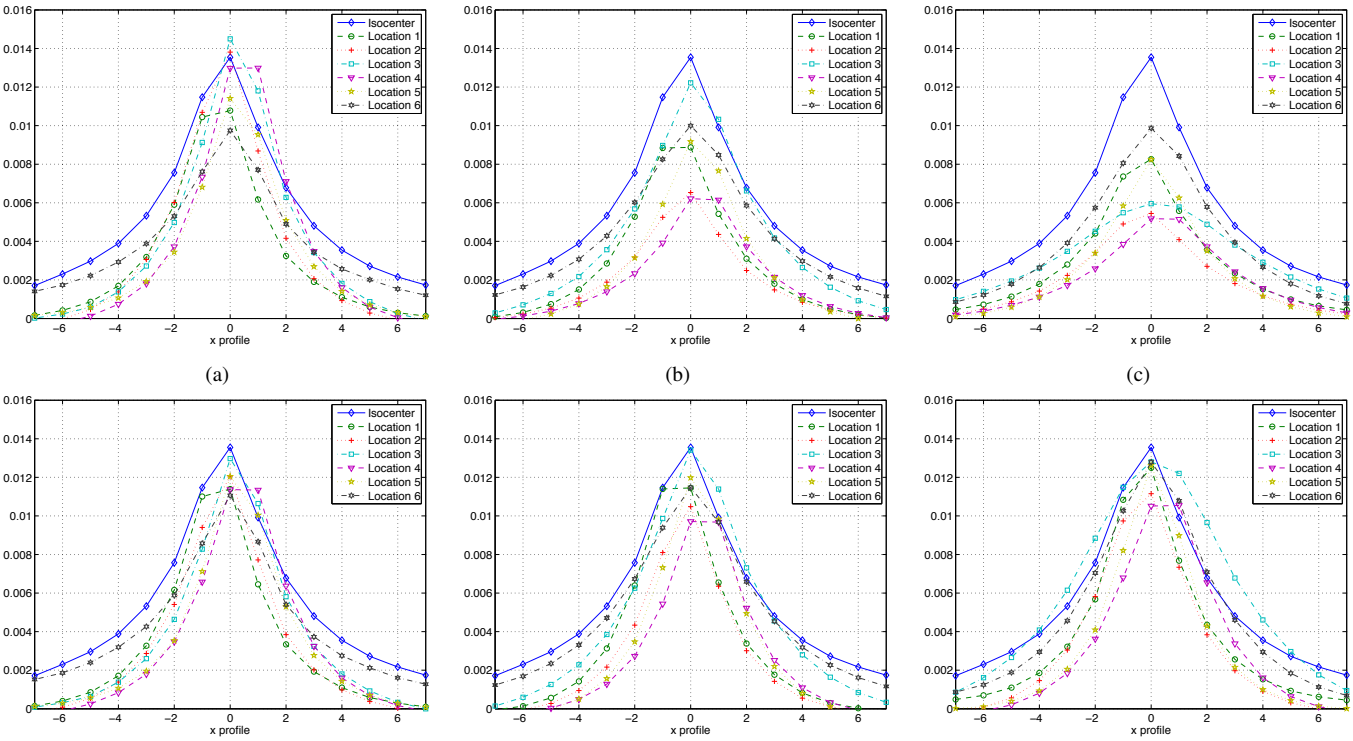

(a) (b) (c)

(d) (e) (f)

Fig. 24. Comparison of x profiles through the center of each local impulse response in Fig. 23. Left column is from a center slice, middle column is from 1st slice of ROI, and right column is from outside of ROI. Top and bottom rows represent the regularizers A-REG (6) and the proposed R-REG-2 (62), respectively. (a) A-REG, center slice (b) A-REG, 1st slice of ROI (c) A-REG, outside ROI (d) R-REG-2, center slice (e) R-REG-2, 1st slice of ROI (f) R-REG-2, outside ROI.

supplement, which led to new expressions for the proposed regularizers. These new regularizers, R-REG-2 and N-REG-2, showed comparable performances in terms of achieving uniform spatial resolution or noise properties in the reconstructed image compared to those presented in [1], R-REG-1 and N-REG-1. It is hard to conclude which factorization is a better choice because R-REG-1 and N-REG-2 obtained better resolution and noise uniformities compared to R-REG-2 and N-REG-1, respectively.

We also investigated a compromise regularizer as a starting point for investigating the trade-off between spatial resolution and noise. The proposed regularizer obtained somewhat balanced spatial resolution and noise properties. However, such compromise regularizers require more detailed investigation.

REFERENCES

[1] J. H. Cho and J. A. Fessler, "Regularization designs for uniform spatial resolution and noise properties in statistical image reconstruction for 3D x-ray CT," *IEEE Trans. Med. Imag.*, 2014, to appear.

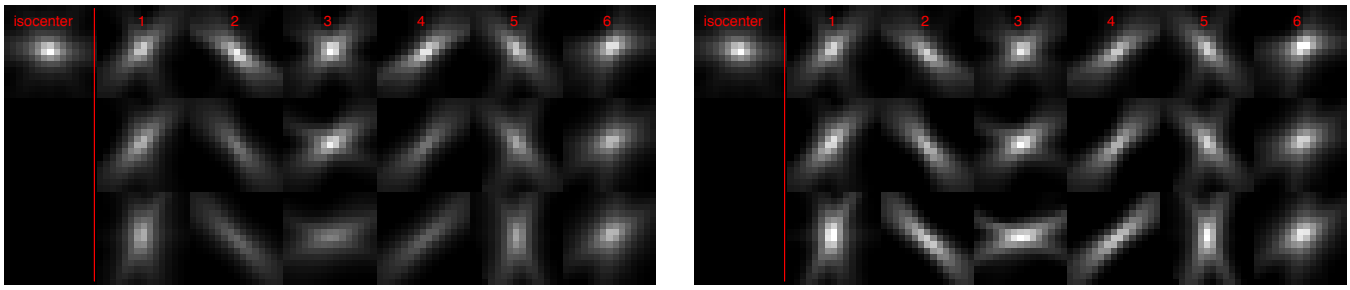

(a) A-REG (b) R-REG-2

Fig. 25. Comparison of xy plane through the center of each local impulses responses at selected location (see Fig. 1 in [1] for the index of locations). Edge-preserving penalty function was used. Top row is from a center slice (blue line in Fig. 1 in [1]), middle row is from 1st slice of ROI (red line), and bottom row is from outside ROI (green line). (a) Regularization with original aggregated certainty (6)] (A-REG) (b) Regularization with proposed pre-tuned spatial strength (62) (R-REG-2).

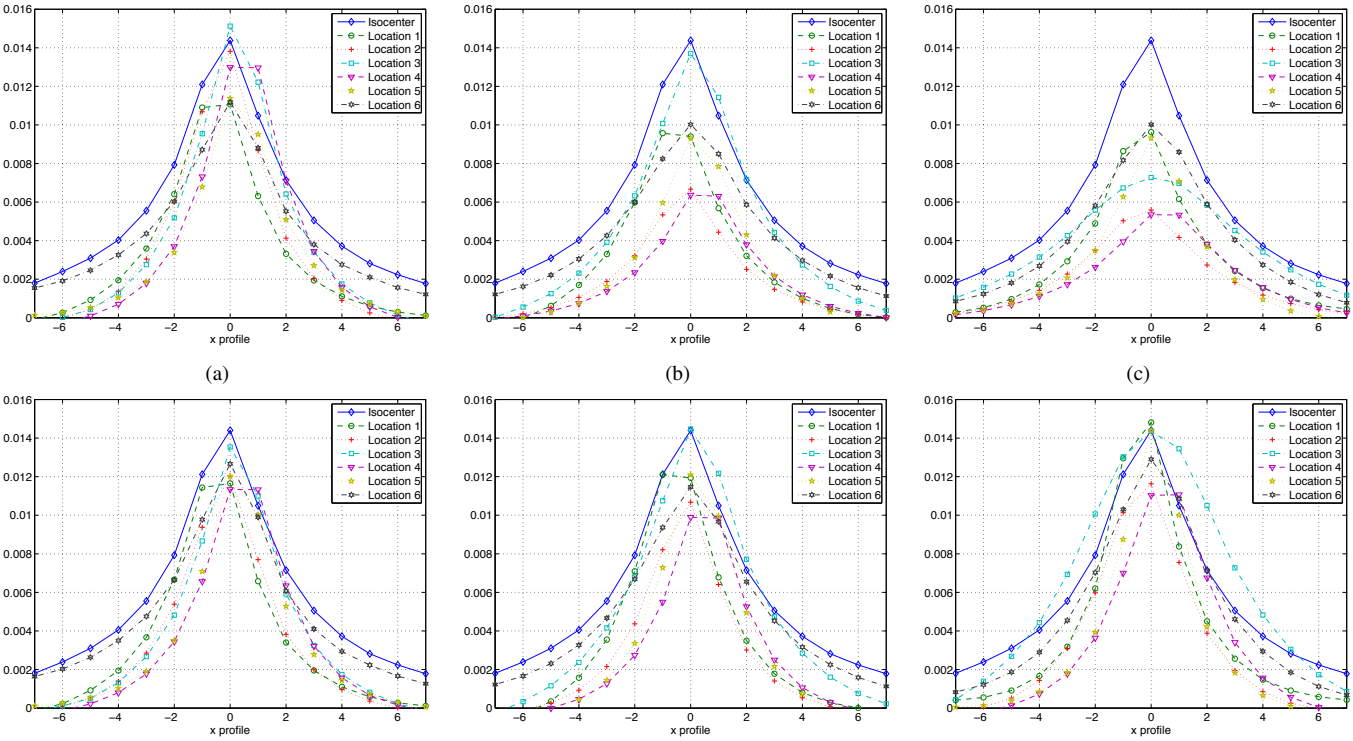

(a) (b) (c)

(d) (e) (f)

Fig. 26. Comparison of x profiles through the center of each local impulse response in Fig. 25. Left column is from a center slice, middle column is from 1st slice of ROI, and right column is from outside of ROI. Top and bottom rows represent the regularizers A-REG (6) and the proposed R-REG-2 (62), respectively. (a) A-REG, center slice (b) A-REG, 1st slice of ROI (c) A-REG, outside ROI (d) R-REG-2, center slice (e) R-REG-2, 1st slice of ROI (f) R-REG-2, outside ROI.